



HAL
open science

MISOLFA: a generalized monitor for daytime spatio-temporal turbulence characterization

Rabah Ikhlef, Thierry Corbard, Frédéric Morand, Catherine Renaud, Maamar Fodil, Aziz Ziad, Julien Borgnino, Mustapha Meftah, Pierre Assus, Bertrand Chauvineau, et al.

► To cite this version:

Rabah Ikhlef, Thierry Corbard, Frédéric Morand, Catherine Renaud, Maamar Fodil, et al.. MISOLFA: a generalized monitor for daytime spatio-temporal turbulence characterization. *Monthly Notices of the Royal Astronomical Society*, 2016, 458 (1), pp.517-530. 10.1093/mnras/stw242 . insu-01275104

HAL Id: insu-01275104

<https://insu.hal.science/insu-01275104v1>

Submitted on 12 Nov 2020

HAL is a multi-disciplinary open access archive for the deposit and dissemination of scientific research documents, whether they are published or not. The documents may come from teaching and research institutions in France or abroad, or from public or private research centers.

L'archive ouverte pluridisciplinaire **HAL**, est destinée au dépôt et à la diffusion de documents scientifiques de niveau recherche, publiés ou non, émanant des établissements d'enseignement et de recherche français ou étrangers, des laboratoires publics ou privés.

MISOLFA: a generalized monitor for daytime spatio-temporal turbulence characterization

R. Ikhlef,^{1,2★} T. Corbard,¹ F. Morand,¹ C. Renaud,¹ M. Fodil,² A. Ziad,¹ J. Borgnino,¹ M. Meftah,³ P. Assus,¹ B. Chauvineau,¹ A. Hauchecorne,³ P. Lesueur,³ G. Poiet,³ F. Ubaldi,¹ M. Hamadouche⁴ and T. Abdelatif²

¹Laboratoire Lagrange, UMR7293, Université Côte d'Azur, Observatoire de la Côte d'Azur (OCA), CNRS, Bd. de l'Observatoire CS 34229, F-06304 Nice Cedex 4, France

²Centre de Recherche en Astronomie Astrophysique et Géophysique (CRAAG), Observatoire d'Alger, 16340, Algiers, Algeria

³Université Versailles St-Quentin; Sorbonne Universities, UPMC Univ. Paris 06; CNRS/INSU, LATMOS-IPSL, 11 Boulevard D'Alembert, F-78280 Guyancourt, France

⁴Université M'Hamed Bougara Boumerdes (UMBB), 35000 Boumerdes, Algeria

Accepted 2016 January 27. Received 2016 January 18; in original form 2015 October 21

ABSTRACT

Ground-based solar observations are strongly affected by optical turbulence. The concept of a new instrument which allows one to measure both spatial and temporal parameters of atmospheric turbulence has been proposed in the late 1990s. The instrument MISOLFA (Moniteur d'Images Solaire Franco-Algérien) is based on this concept and has been developed over the past 10 years in the framework of a ground-based solar astrometry programme and in parallel to the development of several night time turbulence monitors at Calern Observatory, south of France. In this paper, we first describe its instrumental concept, the technical choices that were made to meet the specifications and discuss the difficulties encountered. Using numerical simulations, we present and test the methods that can be used in order to estimate the turbulence parameters from both MISOLFA image and pupil planes. The effect of finite outer scale on Fried parameter estimation from a simple estimate of the angle-of-arrival variance is clearly shown. Finally, we present the first results obtained with the instrument fully operating in its two observing planes. We obtained a mean value of angle-of-arrival coherence time of 5.3 ms, and good agreement is found between spatial parameters obtained with image and pupil planes. First estimates of the atmospheric structure constant $C_n^2(h)$ and outer scale $L_0(h)$ profiles are also presented which illustrates the profiling capacities of the new instrument.

Key words: atmospheric effects – site testing – telescopes – Sun: general.

1 INTRODUCTION

The wavefront of light propagating through earth atmosphere is randomly perturbed due to atmospheric turbulence. Angle-of-arrival (AA) fluctuations, which are fluctuations of the normal to the perturbed wavefronts, are commonly studied to characterize the degree to which turbulence affects ground-based astronomical observations. Several parameters describing the mean spatio-temporal properties of turbulence can be derived from the records of these AA-fluctuations. It is useful to first recall the definitions of these parameters.

(1) The atmospheric structure constant of the air refractive index fluctuations $C_n^2(h)$ showing the turbulence energy distribution with altitude.

(2) The outer scale vertical profile $L_0(h)$ which represents the distribution for the characteristic scale of the largest velocity inhomogeneities in turbulent layers. This parameter is strictly related to the turbulent energy in each layer (Borgnino 1990).

(3) Fried parameter r_0 (Fried 1965) which is the diameter of the coherence zone of the degraded wavefront. It corresponds also to the image resolution obtained with the telescope of diameter r_0 placed outside the atmosphere.

(4) The spatial coherence outer scale \mathcal{L}_0 which defines the maximal size of wavefront perturbations remaining coherent. It traduces the low-frequency evolution of the wavefront and affects long baseline or large telescope observations. \mathcal{L}_0 is an estimator related to

*E-mail: rabah.ikhlef@oca.eu

the optical quality of the perturbed wavefront. For a single turbulent layer, \mathcal{L}_0 is equal to L_0 of that layer (Borgnino 1990).

(5) The isoplanatic patch θ_0 which is the angle where phase or speckles remain correlated.

(6) The correlation time τ_0 which is the time during which the atmosphere may be considered as frozen for the considered structures (phase, speckles), i.e. the time during which they keep their coherence.

For night time observations, several instruments were developed. The most used method consist in analysing fluctuations of a star position with a differential method for estimating Fried parameter r_0 , case of the Differential Image Motion Monitor (DIMM; Sarazin & Roddier 1990) or the four parameters r_0 , \mathcal{L}_0 , θ_0 and τ_0 with the Generalized Seeing Monitor (GSM; Martin et al. 1994; Ziad et al. 2000). Other instruments such as the Monitor of Outer Scale Profile (MOSP; Maire et al. 2007) or, more recently, the Profiler of the Moon Limb (PML; Ziad et al. 2013) analyse the AA-fluctuations by the observation of the lunar limb. However, for daytime atmospheric turbulence, few instruments were developed such as the Solar Differential Image Motion Monitor (S-DIMM; Beckers 2001) for seeing measurements and the Shadow Band Ranger SHABAR for estimating the atmospheric structure constant $C_n^2(h)$ (Beckers 1999, 2001). They provide useful information on the spatial scales of turbulence and are commonly associated for site testing campaigns (Beckers & Mason 1998; Beckers 2001; Liu & Beckers 2001; Berkefeld et al. 2010). The need for high-resolution solar observations from ground has led to the development of multi-conjugate adaptive optics systems for solar observatories. In order to build such system, information about the statistical properties of turbulence as a function of height is needed (Kellerer et al. 2012; Schmidt et al. 2014). Using Shack–Hartmann (SH) sub-apertures as S-DIMM can provide r_0 estimates (Kawate et al. 2011). Furthermore, the measurement of the covariance of differential image displacements at different field angles for pairs of sub-apertures can provide C_n^2 profiles (Scharmer & van Werkhoven 2010).

By recording AA-fluctuations over a given angular extent of the solar limb, MISOLFA (Moniteur d’Images Solaire Franco-Algérien) also provides such profiling capability from its image way. In many situations however, estimates of atmospheric turbulence characteristic temporal scales τ_0 are also needed in order to properly model the effects of the instantaneous equivalent point spread function (PSF) of the instrument through the atmosphere. In the case of solar astrometric measurements using equal-altitude method (solar astrolabe, Laclare 1983; DORAYSOL, Morand et al. 2010), the solar diameter estimates revealed a dependence with the seeing conditions represented by Fried parameter r_0 (Irbah et al. 1994). It has been established that optical turbulence introduces a bias in the estimated position of the inflexion point of the limb-darkening function, the apparent diameter being smaller for bad seeing conditions (Lakhal et al. 1999). This bias also shows weak dependence on the outer scale L_0 for a small-aperture telescope [case of the solar astrolabe $D = 10$ cm in Lakhal et al. (1999)]. Besides this systematic effect, random errors are also introduced by optical turbulence. They decrease with the seeing but are also strongly conditioned by turbulence AA-coherence times (see Lakhal et al. 1999, fig. 2). The coherence time plays also an important role for the optimization of adaptive optics systems; corrections must be faster than the wavefront evolution. In the case of SH sensors used in the adaptive optics systems, AA-fluctuations are directly observed in the image plane. It has been shown however that these fluctuations

can also be recorded in the pupil plane through the analysis of the so-called *flying shadows* (Borgnino & Martin 1977).

The concept of the generalized daytime turbulence monitor MISOLFA is based on the idea that a single instrument could provide both the spatial and temporal turbulence scales by analysing AA-fluctuations simultaneously in its image and pupil ways (Assus et al. 2002; Irbah et al. 2010; Ikhlef et al. 2012b). The instrument has been developed at Calern Observatory and is now operating continuously to monitor daytime turbulence parameters. The estimated spatial parameters are Fried parameter r_0 , spatial coherence outer scale \mathcal{L}_0 , size of the isoplanatic patch θ_0 and optical turbulence profiles from the observation of solar limb. The monitor estimates in the same time AA-characteristic time with its pupil-plane observation way.

Section 2 gives a detailed description of MISOLFA instrument. Section 3 is devoted to the theoretical background and the techniques used for parameter estimation. In Section 4, we describe numerical simulations made to validate the parameter extraction methods, and the first results using the full capacities of the instrument are presented in Section 5.

2 INSTRUMENTAL CONCEPT

In the case of daytime turbulence characterization, except for some particular sites (like Dome C), the only target that is always available is the Sun, which is a spatially extended object. Sunspots may be used as targets for a DIMM but they change their shape and position from a day to another, so the solar limb is generally chosen (Kawate et al. 2011). MISOLFA (Fig. 1) uses both image- and pupil-plane observations to measure turbulence parameters. Its optical layout is presented in Fig. 2. It is based on a Cassegrain coudé telescope of 25.4 cm diameter and an equivalent focal length of 10 m mounted on an alt-azimuthal mount. This mount configuration (alt-az) has been chosen to

- (1) provide a Nasmyth focus, which allows heavier and larger focal instrumentation,
- (2) simplify mechanical conception and realization,
- (3) always keep Sun horizontal edges on the field of the CCD.

After passing through a prismatic entrance window (P1, see section 2.1), the light falls on a concave primary mirror (M1), then is reflected towards a convex secondary mirror (M2). A small tertiary flat mirror (M3) reflects the light to the telescope Nasmyth focus. The derotating prism (P2) allows one to have along the day the two horizontal limbs in a vertical orientation on the camera field. The derotating prism consists of two prisms aluminized and bonded by molecular adhesion, which avoids the alignment problems inherent in conventional derotators made of mirrors. At the telescope output, the focal box contains several optical parts. A filter wheel allows one to select the observation wavelength, and then a beam splitter (P3) divides the optical rays into two ways.

The first one, named in the following *image-plane observation way*, allows one to measure the AA-fluctuations from images of the solar limb recorded on a CCD camera placed on the focal plane (see Fig. 5). Observations taken from this way are similar to those made by MOSP (Maire et al. 2007). The main difference is that the two opposite horizontal solar limbs are observed. They are obtained by the mean of the entrance window (P1), whose principle is shown in Fig. 3(a) and described in Section 2.1.

The second way, named in the following *pupil-plane observation way*, in which the telescope pupil is observed through a lens and



Figure 1. MISOLFA instrument with its entrance window, the alt-azimuthal mount and its focal box on a Nasmyth focus (on the top). In the bottom, we can see the pupil-plane amplification device. The two boxes are connected with optical fibres.

a narrow slit (L1) placed on the solar limb image. This slit is kept perpendicular to the limb thanks to the derotating prism (P2). The slit size is 5 arcsec in the direction parallel to the solar limb (x -direction) and about 25 arcsec in the direction perpendicular to the solar limb (y -direction). The prism (P4) is made of two components, a beam splitter and a reflecting prism of 90° . The two outputs are the pupil image and the global way which integrates the global flux of the pupil focalized by the lens (L2). The pupil image intensity presents fluctuations which are proportional to the AA-fluctuations (see Section 3.1.2). As shown in Fig. 3, optical fibres with different diameters are positioned in the pupil plane to bring light fluctuations to an electronic device. Light fluctuations are then converted to electrical signals by photodiodes. The output signals are very weak; two amplification stages are needed, the first of them is a low-noise amplifier. A National Instruments data acquisition system is then used to record these signals at a rate of 1 kHz. The amplification circuits are shielded and grounded to avoid the effect of parasites such as 50 Hz and the acquisition is connected to the computer via a fibred USB cable.

Due to the important focal length of the telescope (10 m), the guiding system of the alt-az mount was very complex. We developed a fine guiding system based on a solar limb detector algorithm which provides, in near real time, the location of that particular limb point that corresponds to the solar radius which is parallel to the CCD x -axis. This point can be found inside or outside the CCD frame and the goal is to act on the guiding system in order to keep it always at the same nominal location on the CCD. This fine

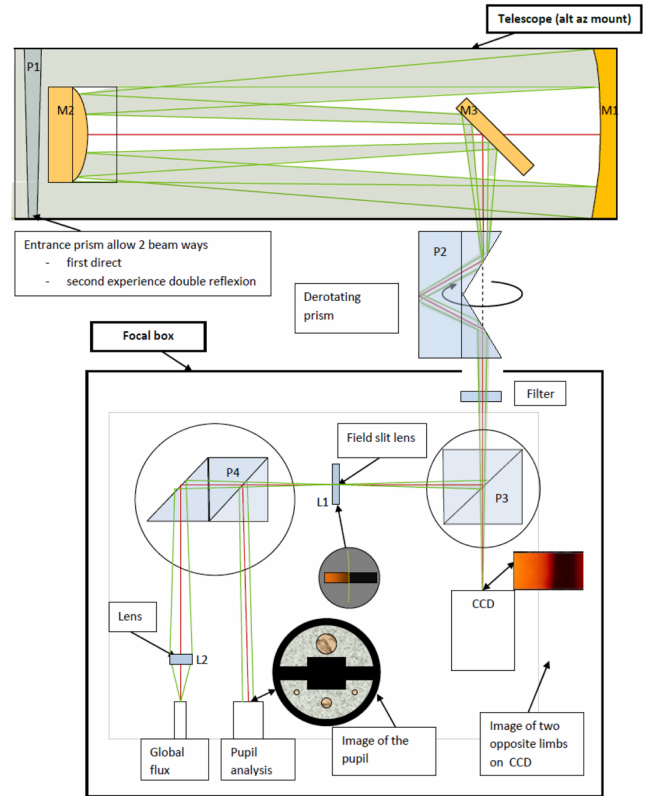


Figure 2. MISOLFA: experimental device. The compact optical configuration allows one to obtain a focal length of about 10 m. The beam splitter (P3) separates the beam into two ways with proportions 30 per cent/70 per cent. In the pupil plane, the use of different diameters allows the detection of different AA-coherence times and also to estimate spatial parameters.

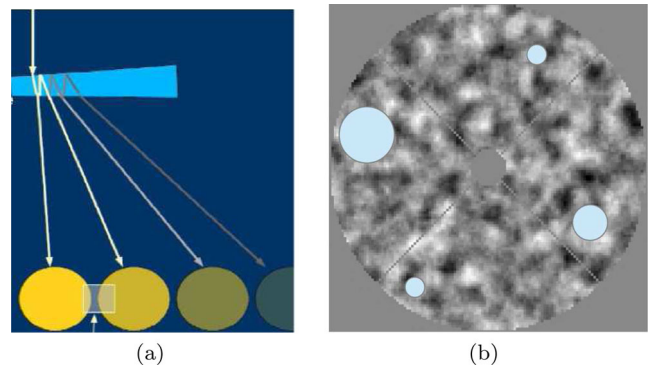


Figure 3. Panel (a) represents the prismatic entrance window allowing one to obtain the two opposite limbs of the solar disc. Separation between the two limbs is most important in summer. Panel (b) shows the optical fibre position on the pupil plane; three diameters are used: 2, 1 and 0.5 mm (two fibres). These values are chosen according to the mean value of Fried parameter recorded at Calern Observatory.

guiding system is only activated between acquisition sequences which last around 1 min and during which we do not want to introduce spurious movements. The components and instrumental parameters of MISOLFA are summarized in Table 1 and, in the following two sections, we discuss in more details the particular choices made for the entrance window and slit dimensions.

Table 1. The Components and instrumental parameters of MISOLFA.

<i>Telescope:</i>	
Model	Cassegrain coudé, Nasmyth focus
Mount	Alt-azimuthal
Aperture	254 mm, $f/40$
Focal length (f_T)	10 m
<i>Prismatic window:</i>	
Prism angle	10 arcmin 54 arcsec
External diameter	270 mm
Internal diameter	256 mm
Thickness	35 mm
<i>Filter:</i>	
Diameter	25.4 mm
Wavelengths	535.7 nm, 607 nm, $\Delta\lambda = 0.5$ nm
<i>CCD Camera:</i>	
Model	PCO PixelFly VGA
Sensor	Sony ICX074AL
Exposure time	1 ms
Frame rate	32 frame/s
Pixel size	9.9 μm (0.2 arcsec)
Number of pixels	640 \times 480
<i>Diaphragm (slit):</i>	
Length	25 arcsec
width	5 arcsec
Lens L1 focal length (f_L)	200 mm
<i>Photodiodes:</i>	
Reference	Hamamatsu S2592-03

2.1 The prismatic entrance window

The goal of MISOLFA is to obtain as maximum as possible information about how turbulence affects solar images and then solar diameter measurements. To separate effects of turbulence from other phenomena such as atmospheric refraction, we chose to estimate turbulence parameters from horizontal solar limbs, i.e. limb points on the solar radii that are parallel to the local horizon. The use of the entrance prism allows one to obtain the two opposite horizontal limbs. However, as shown in Figs 3(a) and 5, the two opposite limbs are not of the same intensity, due to reflections. The three constraints for this optical device were to keep both solar limbs on the CCD at different seasons, to have enough intensity on the reflected image and to keep the intensity ratio between the direct and reflected images stable in time. Because the apparent diameter of the Sun evolves with the season due to the elliptic Earth orbit, the separation between the two images which depends on the prism angle and the angular diameter of the Sun will also be time dependent. The prism angle (see Table 1) was therefore chosen to match this first constraint.

Given the overall transmission of the desired entrance prism (1 per cent), the best theoretical flux ratio of the reflected image to the direct image is 0.8. Several coating methods from different suppliers were tested. Unfortunately, the coatings meeting the specifications were rapidly degraded with time and robust coatings gave a very weak reflected image. The best compromise found between these two criteria has led to a flux ratio of about 0.5 between the two images. With this ratio, it is not possible to have the same quality of turbulence parameter estimates on both sides and, in the following, only the direct images were used. The opposite limb image could however still be used to separate movements due to telescope vibrations or drift, which affect both images in the same way, from the movements of interest induced by turbulence and AA-fluctuations.

2.2 The slit dimensions choice

For an extended source as the Sun, anisoplanatism prevents the use of a simple edge to obtain *solar flying shadows* like for a basic Foucault test. Instead, a thin rectangular slit is used where the two lateral sides limit the angular position observed on the limb and the small side on which the limb is observed performs a Foucault test. However, the use of a diaphragm of finite size in the focal plane introduces additional effects which limit AA-fluctuation analysis from intensity measurements of the pupil-plane images. Two effects were highlighted and have been studied by Borgnino & Martin (1977, 1978). They are related to the diffraction and angular filtering by the diaphragm. First, the presence of a diaphragm with an angular width w_x in the focal plane is equivalent to a high spatial frequency filter with a cut-off frequency f_d given by

$$f_d \approx \frac{w_x}{\lambda}. \quad (1)$$

On the other hand, geometrical considerations allow us to say that details in a turbulent layer located at an altitude h have spatial dimensions on the pupil plane of about hw_x . We can then define a spatial cut-off frequency f_a for the angular filter as

$$f_a \approx \frac{1}{hw_x}. \quad (2)$$

Borgnino & Martin (1977, 1978) have shown that the best compromise is to put $f_a = f_d$. The effect of the two filterings is presented in a synthetic way in Borgnino & Martin (1977, fig. 7). A wheel containing slits of different sizes is installed behind the beam splitter which allows selecting different filtering as a function of altitude. This capacity of our instrument has however not been used so far. For a slit having an angular width equal to 5 arcsec (Table 1) and for observations in the visible (535 nm), the filtering by diffraction is dominating until a height $h = 911$ m. This filtering of the elements lower than 2.2 cm in size is the same whatever is the height from 0 to 911 m. For higher altitudes, the angular filtering becomes dominant.

Finally, the diameters of the four sub-pupils have been chosen equal to 0.5, 1 and 2 mm so that they correspond, respectively, in the entrance pupil, to half, one time and twice a mean value of r_0 of about 3 cm. The position of these sub-pupils is shown in Fig. 3(b).

3 MEASUREMENT PRINCIPLE, THEORETICAL MODELS AND TURBULENCE PARAMETER ESTIMATION

3.1 Theoretical background

3.1.1 The image-plane observation way

In this section, we recall the theoretical basic equations. They are obtained in the same way as those used to interpret the night time observation data given by GSM (Martin et al. 1994; Ziad et al. 2000) and MOSP (Maire et al. 2007). In the case of MISOLFA, observations of the solar limb are performed with a single telescope (pupil of diameter D) in directions on the sky separated by angles θ up to 96 arcsec. The atmospheric turbulence can be described by the Von Kàrmàn model with a coherence inner scale taken equal to zero. The phase power spectrum is related to the turbulence energy and the outer scale distributions with altitude. For each layer at an altitude h_0 (with a thickness δh), the Von Kàrmàn phase power

spectrum is expressed as (Borgnino, Martin & Ziad 1992)

$$W_\phi(f, h0) = 0.38\lambda^{-2} \int_{h_0}^{h_0+\delta h} C_n^2(h) \left[f^2 + \frac{1}{L_0(h)^2} \right]^{-\frac{11}{6}} dh, \quad (3)$$

where f is an angular frequency and λ is the wavelength. We can then introduce the transverse (in the y -direction) AA angular structure function $D_\alpha(\theta)$ which gives an estimation of the AA angular decorrelations. It is expressed in the case of Von K arm an model with a multilayer turbulence as (Borgnino et al. 1992; Avila et al. 1997; Maire et al. 2007)

$$D_\alpha(\theta) = 2.4 \sec(z) \int_0^{+\infty} dh C_n^2(h) \int_0^{+\infty} df f^3 \left(f^2 + \frac{1}{L_0(h)^2} \right)^{-\frac{11}{6}} \times [1 - J_0(2\pi f\theta h) - J_2(2\pi f\theta h)] \left[\frac{2J_1(\pi Df)}{\pi Df} \right]^2, \quad (4)$$

where z is the zenith distance and J_0, J_1, J_2 are Bessel functions of the first kind. This structure function can also be expressed as

$$D_\alpha(\theta) = 2[\sigma_\alpha^2 - C_\alpha(\theta)], \quad (5)$$

where $C_\alpha(\theta)$ is the covariance and $\sigma_\alpha^2 = C_\alpha(0)$ is the variance of AA-fluctuations. If we further assume that it exists an equivalent impulse layer, located at altitude h , giving the same optical effects at ground level as the whole turbulent terrestrial atmosphere (one-layer model), then the transverse angular structure function is given by (Bouزيد et al. 2002; Seghouani, Irbah & Borgnino 2002)

$$D_\alpha(\theta) = 0.1437 \lambda^2 r_0^{-\frac{5}{3}} \int_0^{+\infty} df f^3 \left(f^2 + \frac{1}{L_0^2} \right)^{-\frac{11}{6}} \times [1 - J_0(2\pi f\theta h) - J_2(2\pi f\theta h)] \left[\frac{2J_1(\pi Df)}{\pi Df} \right]^2. \quad (6)$$

3.1.2 The pupil-plane observation way

Geometrical optics is helpful to understand how AA-fluctuations are put in evidence in the pupil plane. Light rays of the atmospheric perturbed wavefront undergo random angles and pass or not through the diaphragm (slit). The pupil illumination observed through the diaphragm will then be related to the local slopes of the wavefront. Intensity variations in the pupil-plane image are therefore directly related to AA-fluctuations at the telescope entrance pupil when an extended source is observed.

Previous works have effectively shown the good linear relationship between intensity fluctuations of flying shadows observed in the pupil plane and AA-fluctuations from theoretical background, numerical simulations and observations (Borgnino & Martin 1977, 1978; Borgnino 1978; Berdja et al. 2004; Borgnino et al. 2007). The formalism explaining this proportional relationship was explained in detail by these authors; we recall hereafter the main ideas. We first consider a monochromatic plane wave (with wavelength λ) passing through atmospheric turbulence. Arriving at the ground, it is characterized by its complex amplitude

$$\psi(\mathbf{r}) = A(\mathbf{r})\exp(\varphi(\mathbf{r})), \quad (7)$$

where $A(\mathbf{r})$ is the amplitude and $\varphi(\mathbf{r})$ is the phase. \mathbf{r} is a vector in planes perpendicular to the optical axis. The AA-fluctuations are defined as the slope of the wavefront phase. For a given point whose coordinates are $\mathbf{r}(x, y)$, the two components of the AA-fluctuations are

$$\alpha(\mathbf{r}) = -\frac{\lambda}{2\pi} \frac{\partial \varphi(\mathbf{r})}{\partial x}$$

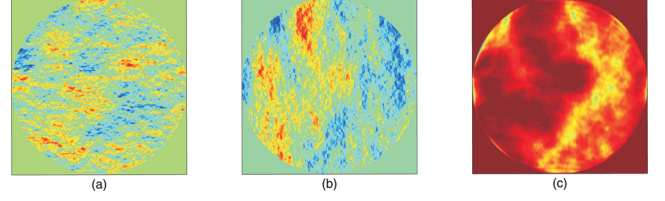


Figure 4. Simulated AA-fluctuations (from the work of Berdja in 2004) computed directly from the perturbed wavefront phase and observed as intensity fluctuations in pupil-plane image. Panels (a) and (b) show, respectively, x and y AA components at the entrance pupil, while panel (c) shows the y component observed in the pupil-plane image as intensity fluctuations. The perturbed wavefront was simulated in the near-field approximation case considering $r_0 = 4$ cm, $L_0 = 10$ m, $h = 1000$ m. The diaphragm width was taken equal to few arcseconds.

$$\beta(\mathbf{r}) = -\frac{\lambda}{2\pi} \frac{\partial \varphi(\mathbf{r})}{\partial y}. \quad (8)$$

We can divide the optical system into two parts. First, a telescope characterized by its pupil function $P(\mathbf{r})$ and a focal length f_T . The second part is a diaphragm through which we observe the image of the telescope entrance pupil and characterized by its transmission function $t(\mathbf{r})$ and the focal length f_L of a lens (L1) placed behind it. Intensity distribution in the obtained pupil image formed by the lens L1 may be obtained according to Fourier optics calculations. If we assume that the limb profile is linear with the angular direction, intensity fluctuations in the pupil image are expressed as a function of $\beta(-\mathbf{r})$, the y component of the AA-fluctuations (Borgnino 1978; Berdja et al. 2004; Borgnino et al. 2007):

$$I_0(\mathbf{r}) = a \frac{f_T}{f_L} \left[\frac{\lambda f_T}{f_L} \right]^2 \left| \hat{t} \left(\frac{\mathbf{r}}{\lambda f_L} \right) \right|^2 * \left[P \left(-\mathbf{r} \frac{f_T}{f_L} \right) \beta \left(-\mathbf{r} \frac{f_T}{f_L} \right) \right], \quad (9)$$

where \hat{t} denotes the Fourier transform and $*$ symbolizes a convolution product; a is a proportionality factor in linear solar limb model.

So, using a linear model of solar limb, the intensity fluctuations in the pupil image vary linearly with the slope of the wavefront observed in the direction perpendicular to this limb (y -direction). The pupil-plane observation way introduces a spatial filtering in the image due to the diaphragm. We therefore measure AA-fluctuations in the y -direction (Fig. 4). Berdja et al. (2004) have shown the good linear relationship between AA-fluctuations and intensity fluctuations as modelled with equation (9) when the solar limb is observed. In fact, we can consider that the limb-darkening profile is almost linear in the small angular field of view allowed by the diaphragm so the hypothesis of linearity remains valid.

3.2 Data analysis and parameter extraction

3.2.1 Image-plane measurements

As described above, the method is based on statistical analysis of AA-fluctuations. For that, to have sufficient samples, data sets consist in series of about 2000 images recorded at a rate of 32 frames per second. According to H. M. Martin, exposure time of the detector is a crucial parameter for seeing studies. It should be shorter than 10 ms to freeze the atmospheric image motion (Martin 1987). Thus, the exposure time of the video CCD camera is adjusted to a constant value of 1 ms. Fig. 5 shows an image of the Sun recorded on 2014 September 09 with this observation way at 607 nm. The pixel size

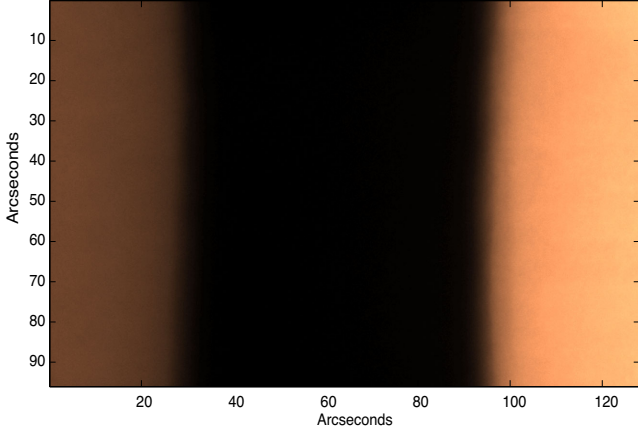


Figure 5. A solar image obtained with the image-plane observation way of MISOLFA. On the left the reflected limb and the direct limb is on the right.

is about 0.2 arcsec which leads to an image size of approximately 96 by 128 arcsec. Each CCD pixel line in the direct and reflected limb images is such as it is located on a direction parallel to the local horizon. For each image, the following processing steps are performed.

(1) Noise estimation using *standard deviation histogram algorithm* (Gao 1993). The estimation of noise is useful for the next step (wavelet denoising).

(2) Image cleaning by wavelet denoising process to eliminate sunspots which can make difficult the limb detection step (Mousaoui & Irbah 2000; Djafer & Irbah 2012).

(3) Limb detection using the second derivative over each line of the CCD. We first apply wavelet denoising on an image, then we compute its horizontal gradient, and finally we apply wavelet denoising on the gradient and a second derivation is performed. By choosing suitable thresholds, limbs are well detected in good observational conditions.

(4) Each limb is then corrected from medium edge (correction from the curvature of the solar limb) to extract at the end only fluctuations due to turbulence.

(5) The above steps are performed to extract AA-fluctuations from temporal series of solar images allowing one to compute the two main output which are the experimental AA transverse covariance function $C_{\alpha_{\perp}\text{Exp}}(\theta)$ (and so the variance) and the structure function $D_{\alpha_{\perp}\text{Exp}}(\theta)$ which equation is given by (Maire et al. 2007)

$$D_{\alpha_{\perp}\text{Exp}}(\theta) = \frac{1}{N} \sum_{i=1}^N \frac{1}{\theta_m - \theta} \sum_{k=1}^{\theta_m - \theta} [\alpha_{\perp}(k) - \alpha_{\perp}(k + \theta)]^2, \quad (10)$$

where θ is the angular separation in pixels, θ_m is the maximal extent accessible in the image (i.e. 480 pixels in our case), N is the number of processed images (about 2000) and $\alpha_{\perp}(k)$ is the AA-fluctuations retrieved at the position k . To get a statistical convergence, the number N of short exposure images to be considered has to be as large as possible within the time the atmosphere keeps the same statistical properties. This time is expected to be greater than the 1 min duration of our sequences (Sarazin & Roddier 1990). In the case of the DIMM experiment, the total number of samples considered for image motion variance estimation is about 200 (Sarazin & Roddier 1990) or 300 for the ATST site testing campaign (Beckers, Liu & Jin 2003). The relative statistical error on the variance is equal to $\sqrt{\frac{2}{n-1}}$. $n = 2000$ images will give a 2 per cent relative error on r_0

(proportional to $\sigma^{-3/5}$) and less than that for different points of the structure function ($n = 2000(\theta_m - \theta)$; Maire et al. 2007). Increasing N within the coherence time of seeing will reduce the relative statistical error but we are limited by the CCD transfer delay and the hard disks storage (1.2 Gb for each series).

Using numerical simulations, Berdja (2007) has shown that AA-fluctuations are also proportional to photometric integral variation with suitable thresholding near the limb over a series of successive images. According to the author, this method should be less sensitive to noise than estimating the position of the zero crossing of the second derivative of the limb profile. In practice, this method can effectively be used to provide a quick proxy of fluctuations σ_{α}^2 but is not able to reliably provide the full structure function.

Considering equation (4) and using a subsequent non-linear fit, one can retrieve the $C_n^2(h)$ and $L_0(h)$ profiles together by minimizing the cost function (Maire et al. 2007): $E = \sum_{\theta} [D_{\alpha_{\perp}\text{Exp}}(\theta) - D_{\alpha_{\perp}Th}(\theta)]^2$, where $D_{\alpha_{\perp}Th}(\theta)$ is the theoretical structure function in equation (4). The Levenberg–Marquardt method is used in our case; limits are assumed for the parameters in order to obtain realistic values and to reduce convergence time to the optimal solution.

The integrated parameters Fried parameter r_0 , the spatial coherence outer scale \mathcal{L}_0 , the altitude of the equivalent impulse layer H and the isoplanatic angle θ_0 are then estimated using the following equations (Roddier 1981; Maire et al. 2007):

$$r_0 = \left[0.423 \left(\frac{2\pi}{\lambda} \right)^2 \sec(z) \int dh C_n^2(h) \right]^{-5/3} \quad (11)$$

$$\mathcal{L}_0 = \left[\frac{\int dh C_n^2(h) L_0(h)^n}{\int dh C_n^2(h)} \right]^{1/n} \quad (12)$$

$$H = \sec(z) \left[\frac{\int dh C_n^2(h) h^{5/3}}{\int dh C_n^2(h)} \right]^{3/5} \quad (13)$$

and

$$\theta_0 = 0.31 \frac{r_0}{H}, \quad (14)$$

where the factor n in equation (12) varies according to the instrument which measures the integrated parameter \mathcal{L}_0 . Borgnino (1990) found that for AA-fluctuations $n = -1/3$ is appropriate, whereas Maire et al. (2007) suggested another value $n = 11/3$ to match between MOSP and GSM measurements. We took $n = 11/3$ because MISOLFA is similar to MOSP.

In a particular case of a dominant layer at a given altitude, one can consider the one-layer model of equation (6) to retrieve the three parameters r_0 , \mathcal{L}_0 and the altitude of dominant layer h using a non-linear fitting.

The Fried parameter r_0 can also be estimated from the variance of AA-fluctuations σ_{α}^2 which is the first value of the covariance ($C_{\alpha}(0)$) according to a given model. If one consider Von Kàrmàn model, r_0 is related to AA variance by the following expression (Ziad et al. 1994):

$$r_{0v} = 8.25 \cdot 10^5 \lambda^{6/5} \sigma_{\alpha}^{-6/5} \left[D^{-1/3} - 1.525 \mathcal{L}_0^{-1/3} \right]^{3/5}, \quad (15)$$

where σ_{α} is expressed in arcseconds.

This equation takes into account the effect of a finite outer scale. The estimation method (from limb motion) is very sensitive to telescope vibration and wind. The use of the full structure function equation (6) should be more robust with this respect. Another possibility would be to use a differential estimation (Fried 1975; Acton

1995) like in the S-DIMM or PML instruments. As we will see in the next section, MISOLFA pupil way can also be used to retrieve r_0 by using two sub-pupils of the same diameter which is also a form a differential estimation. We note that for large values of the outer scale \mathcal{L}_0 , equation (15) reduces to the Kolmogorov model for r_0 estimation (Borgnino et al. 1982; Irbah et al. 1994):

$$r_0 = 8.25 \cdot 10^5 \lambda^{\frac{6}{5}} D^{-\frac{1}{5}} \sigma_\alpha^{-\frac{6}{5}}. \quad (16)$$

3.2.2 Pupil-plane measurements

The main purpose of observing intensity fluctuations at high cadence (1 KHz) in the pupil plane is to estimate the turbulence AA-coherence time. However, it is also possible to reach again the spatial parameters (r_0 and L_0). Four photodiodes allow one to record the intensity fluctuations with optical fibres positioned on the image behind diaphragms of different sizes (2, 1 and 0.5 mm diameter); a fifth photodiode behind a fibre of 2 mm diameter integrates the global flux of the whole pupil plane. This later signal is used to separate the AA-fluctuations from intensity fluctuations due to scintillation and other effects. This kind of correction is similar to a flat-field in the image plane. The corrected signals given by the four photodiodes are recorded simultaneously and a spatio-temporal analysis is performed.

Temporal covariance functions (and temporal structure functions) are obtained by autocorrelation of the signals. To obtain the characteristic time, each signal is divided into portions of 100 ms each, then the temporal structure function is obtained by the same way as equation (10) replacing the angular separation θ by the sampling time. The temporal characteristic time τ_0 is obtained from temporal covariance (or from temporal structure functions). It is defined as the time for which the covariance decreases from the origin by a factor k or using the structure function as the time of the drop of a constant k' from the saturation of the AA-temporal structure function (Ziad et al. 2012).

In practice, once the temporal structure function is obtained from intensity fluctuations of a given sub-pupil, we fit it by a function of the form

$$F(t) = A_{\max} (1 - e^{-t/\tau}). \quad (17)$$

Using this function, the characteristic time τ_0 is thus the corresponding time to the A_{\max}/k' (generally k' is taken equal to e).

The spatial coherence parameters r_0 and \mathcal{L}_0 may be obtained from the pupil-plane observation way together with AA-fluctuation characteristic times. The structure function of AA-fluctuations recorded by mean of a pair of photodiodes of the same size positioned in the pupil image may be expressed as (Sarazin & Roddier 1990; Borgnino et al. 2007)

$$D_\alpha(S) = 0.364 \left[1 - 0.541 \left(\frac{S}{D_p} \right)^{-\frac{1}{3}} \right] \lambda^2 r_0^{-\frac{5}{3}} D_p^{-\frac{1}{3}}, \quad (18)$$

where S is the baseline formed by the two photodiodes of the same integration size D_p . The structure function $D_\alpha(S)$ is expressed in arc-seconds. equation (18) will be used to calculate r_0 . This involves the computation of the difference between the variance and the covariance between the two sub-pupils (cf. equation 5). This expression does not depend on \mathcal{L}_0 .

On the other hand, the ratio between the covariance and variance, called also the normalized covariance, does not depend on r_0 (Avila

et al. 1997),

$$\Gamma_\alpha = \frac{C_\alpha(S, D_{p1}, \mathcal{L}_0)}{\sigma_\alpha^2(D_{p1}, \mathcal{L}_0)}. \quad (19)$$

This ratio remains a function of the baseline S and the diameter but is no longer dependent on r_0 because both the variance and covariance are proportional to $r_0^{-5/3}$. \mathcal{L}_0 is determined numerically from this equation by using the asymptotic expressions of covariance and variance (Conan 2000; Conan et al. 2000):

$$C_\alpha(S, D_p, \mathcal{L}_0) = 0.0589 \lambda^2 r_0^{-\frac{5}{3}} D_p^{-\frac{1}{3}} \left[-3.001 \left(\frac{\pi D_p}{\mathcal{L}_0} \right)^{\frac{1}{3}} - 1.286 \left(\frac{\pi D_p}{\mathcal{L}_0} \right)^{\frac{7}{3}} + \left(\frac{S}{D_p} \right)^{-\frac{1}{3}} (5 - \cos(2\gamma)) \right. \\ \left. \times \left[0.411 + 0.188 \left(\frac{\pi D_p}{\mathcal{L}_0} \right)^2 \right] \right], \quad (20)$$

where putting $\gamma = \frac{\pi}{2}$ gives the transverse component of the covariance whereas $\gamma = 0$ corresponds to the longitudinal one (Avila et al. 1997). And

$$\sigma_\alpha^2(D_p, \mathcal{L}_0) = 0.1697 \lambda^2 r_0^{-\frac{5}{3}} D_p^{-\frac{1}{3}} \left[1 - 1.041 \left(\frac{\pi D_p}{\mathcal{L}_0} \right)^{\frac{1}{3}} + 0.565 \left(\frac{\pi D_p}{\mathcal{L}_0} \right)^2 - 0.446 \left(\frac{\pi D_p}{\mathcal{L}_0} \right)^{\frac{7}{3}} \right]. \quad (21)$$

If we consider the case for which \mathcal{L}_0 is large in regard to D_p , this expression becomes (Ziad et al. 1994)

$$\sigma_\alpha^2(D_p, \mathcal{L}_0) = 0.1697 \lambda^2 r_0^{-\frac{5}{3}} \left[D_p^{-\frac{1}{3}} - 1.525 \mathcal{L}_0^{-\frac{1}{3}} \right]. \quad (22)$$

One can see from variance equation (22) that it is, in principle, possible to estimate the \mathcal{L}_0 parameter when Fried parameter is known. But this method is sensitive to errors in r_0 estimation.

Finally, we note that \mathcal{L}_0 may also be obtained from equation (22) applied to two photodiodes of different area integration sizes D_{p1} and D_{p2} . In this case, it is also possible to compute a ratio $R_{\mathcal{L}_0}$ involving only the two variances and which is independent from r_0 (Ziad et al. 1994):

$$R_{\mathcal{L}_0} = \frac{\sigma_\alpha^2(D_{p1}, \mathcal{L}_0) - \sigma_\alpha^2(D_{p2}, \mathcal{L}_0)}{\sigma_\alpha^2(D_{p1}, \mathcal{L}_0)} = \frac{D_{p1}^{-\frac{1}{3}} - D_{p2}^{-\frac{1}{3}}}{D_{p1}^{-\frac{1}{3}} - 1.525 \mathcal{L}_0^{-\frac{1}{3}}}. \quad (23)$$

Borgnino et al. (2007) advocate that the ratio between the diameters of the two sub-pupils should be at least equal to 3. In practice, we were unable to use this approach with our current setting, the sizes of our sub-pupils are probably too close and the signal-to-noise ratios of the different sub-pupils are too different.

4 NUMERICAL SIMULATIONS

The step of numerical simulation is very important while doing physical measurements. It allows one to see the response of a system while varying input parameters and eventually to select an appropriate model describing a physical phenomenon. We performed numerical simulations to verify the feasibility of parameter extraction method. Another important goal of these simulations is to obtain error bars on the measured parameters.

These simulations can be divided into three steps: image simulation without turbulence, turbulent wavefront generation and obtention of perturbed images. Then the same processing steps as for real

data can be applied. Berdja et al. (2004) have done numerical simulations related to the pupil-plane observation way and have shown excellent agreement between input AA-fluctuations and intensity fluctuations in the pupil. Here we are interested in the image plane.

First, simulation of solar image (without turbulence) with the appropriate sampling ($0.2 \text{ arcsec pixel}^{-1}$ as MISOLFA images) is made using a limb-darkening model. We used the model proposed by Hestroffer & Magnan (1998, HM98) at a wavelength equal to 535 nm.

A disturbed turbulent wavefront is then generated which is due to a single layer at a given altitude and characterized by spatial parameters r_0 and \mathcal{L}_0 . The most common method for phase screen generation is based on Fourier transform (Nakajima 1988; Schmidt 2010). The phase from this method is obtained by the inverse Fourier transform of the spectral phase density calculated according to the Von K arm an model. We assume that the optical effect induced by the whole atmosphere is equivalent to the effect of a single layer at an altitude h . The sub-harmonics method is implemented to compensate the poorness of the spectral density in lower spatial frequencies.

Special attention must be given to the sampling of the generated phase screen. If L_x and L_y are the dimensions of the screen, choosing a spatial sampling δx will impose a maximum frequency sampling $f_{\text{max}} = 1/2\delta x$ in the x -direction and the number of points N_x will define the frequency sampling $df = 2f_{\text{max}}/N_x$. Constraints are applied while choosing these quantities; we will see them next.

If the turbulence is characterized by spatial parameters: r_0 and \mathcal{L}_0 , the size of the perturbed phase screen L_x (and L_y) is chosen very much larger than \mathcal{L}_0 and the spatial sampling must stay much lower than r_0 . The disturbed solar image is obtained by a convolution between the simulated Sun image and the pupil+atmosphere equivalent PSF. The angular limitation by a $N_p \times N_p$ pupil introduces an angular sampling on the resulting PSF defined by

$$\Delta\theta = \frac{\lambda}{N_p \delta_x}, \quad (24)$$

where δ_x is the spatial sampling step on the pupil. We have now two cases: isoplanatic and anisoplanatic imaging.

First we have the case of isoplanatism, in which we suppose that all the rays coming from an object pass through the same turbulence. This is equivalent to a turbulence localized at ground level ($h = 0$). In this case, one can obtain the resulting perturbed image by a direct convolution with a unique PSF.

In the case of anisoplanatism, simulation is made by generating a PSF for every incident angle of the angular domain allowed by the entrance pupil sampled by $\Delta\theta$. This is made by displacing the pupil on the phase screen (localized at an altitude h) by a step $dr = h\Delta\theta$. A convolution product is performed for each point of the object to obtain the corresponding point on the resulting image. Fig. 6 shows an example image obtained in this way. A series of 1000 images are simulated by randomly generating phase screens with the same input parameters (r_0 , \mathcal{L}_0 and h). The resulting images are processed following the same steps: edge detection, covariance and structure functions computing, non-linear curve fitting according to the Von K arm an model and using Levenberg–Marquardt method. The whole process is repeated to achieve a Monte Carlo simulation allowing us to obtain mean values and standard deviations.

For a turbulence characterized by spatial parameters $r_0 = 6.5 \text{ cm}$, $\mathcal{L}_0 = 3 \text{ m}$ and $h = 3500 \text{ m}$, we obtained the structure function given by Fig. 7. The value of \mathcal{L}_0 has been chosen relatively small compared to night time values and we took it very small to see the result of neglecting its effect. Because turbulence is generated

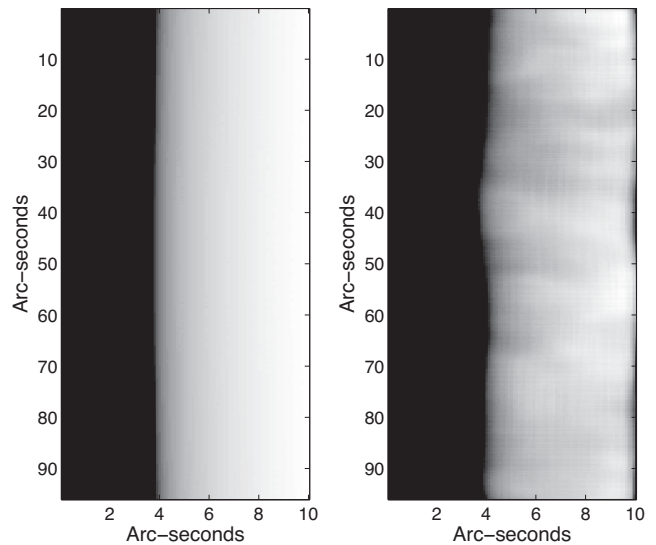


Figure 6. Simulated MISOLFA images. Left image is obtained using limb-darkening function described by the HM98 model. The right image is the result of anisoplanatic imaging through the one-layer turbulent wavefront characterized by $r_0 = 6.5 \text{ cm}$, $\mathcal{L}_0 = 3 \text{ m}$, $h = 3500 \text{ m}$.

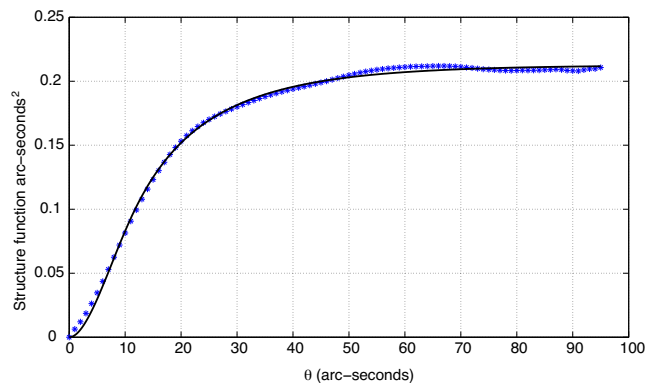


Figure 7. Simulated (stars) AA-structure function obtained by simulations in image plane and its non-linear fit by theoretical one (solid line, obtained using equation 6). The perturbed wavefront was simulated considering $r_0 = 6.5 \text{ cm}$, $\mathcal{L}_0 = 3 \text{ m}$, $h = 3500 \text{ m}$.

with a single layer, equation (6) can be directly used to extract parameters by a non-linear fit. From structure function in Fig. 7, the extracted parameters are (mean values and standard deviations through 20 realizations) $r_0 = 6.8 \pm 0.8 \text{ cm}$, $\mathcal{L}_0 = 3.4 \pm 1.3 \text{ m}$ and $h = 4617 \pm 470 \text{ m}$.

For the structure function of Fig. 7, inverting equation (4) by a non-linear iterative fit gives the $C_n^2(h)$ profile (mean profile through 20 realizations) of Fig. 8 and the outer scale profile. The grid resolution in altitude is 100 m. Equations (11) through (14) allow one to estimate the values: $r_0 = 6.5 \pm 0.4 \text{ cm}$, $\mathcal{L}_0 = 3.7 \pm 1.7 \text{ m}$, the equivalent altitude $H = 3503 \pm 60 \text{ m}$ and $\theta_0 = 1 \pm 0.1 \text{ arcsec}$ which are in excellent agreement with the input values. Fig. 8 shows a dominant layer localized at an altitude of 3500 m as expected. Another effect has been studied by the simulations. Observations made with telescopes suffer from vibrations, drift in mount tracking and wind effect. All these parameters will make image motion contaminated by noise, i.e. motions that are not due to turbulence. To simulated solar edges, we have intentionally added a drift which was

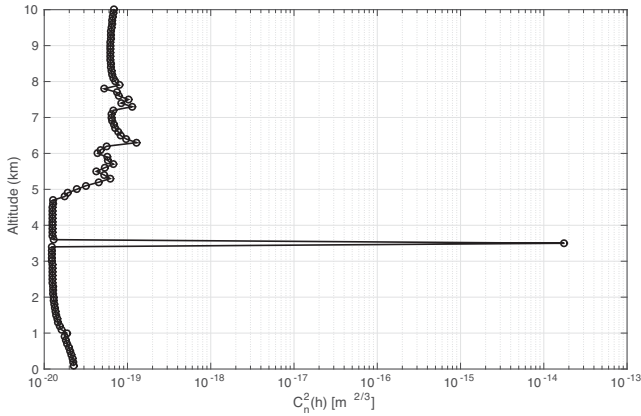


Figure 8. C_n^2 profile retrieved (using equation 4) from the structure function obtained by simulation in image plane. The perturbed wavefront was simulated considering one layer characterized by $r_0 = 6.5$ cm, $\mathcal{L}_0 = 3$ m and localized at an altitude $h = 3500$ m.

chosen to be representative of the observed drifts with MISOLFA. Before doing AA-fluctuation structure function computation, summits of parabolas fitting each image edge have been estimated. A polynomial fit was then applied to the temporal evolution of the resulting summits and subtracted from each limb edge. While computing the structure function, correction from mean limb is made every 100 images. The resulting structure function non-linear fitting using steps described above gave spatial parameters: $r_0 = 6.8 \pm 1.2$ cm, $\mathcal{L}_0 = 3.1 \pm 1.3$ m and $h = 4617 \pm 980$ m using the one-layer model. These values are in good agreement with input parameters except for h . Considering the multilayer model, the retrieved profiles give the following integrated parameters: $r_0 = 6.3 \pm 0.5$ cm, $\mathcal{L}_0 = 3.7 \pm 2.2$ m and $H = 3630 \pm 125$ m. As a conclusion, usual drift effect can be considered as compensated by this technique which is employed to process data from image-plane observation way of MISOLFA. Of course, unusual jumps or strong drifts due to wind or anomalous instrumental effects still need to be detected and processed separately.

In order to check the case of multiple layers, we simulated the anisoplanatic imaging through two turbulent layers localized respectively at 3500 and 7000. The fractional turbulence energies were chosen to be 0.7 and 0.3, respectively, with an integrated Fried parameter of 6.5 cm and $\mathcal{L}_0(h) = 3$ m for the two layers. The resulting $C_n^2(h)$ profile is given by Fig. 9. The two layers are put in evidence in the retrieved profile and the resulting integrated parameters for that realization are $r_0 = 6.6$ cm, $\mathcal{L}_0 = 4.3$ m and $H = 4900$ m. The fractional energies of the two layers in the retrieved $C_n^2(h)$ profile are 0.62 and 0.38. We note that, like in the more general multiple-layer case, the solution of the two-layer case is not unique. If both the heights of the two layers and the amplitudes of the outer scale and structure constant are left without constraint, i.e. a priori knowledge, it is possible to find layers at different altitudes that will reproduce equally well the structure function. In the example discussed here, the heights of the layers and the amplitudes of the structure constant were left free of constraints but an a priori on the outer scale was introduced by bounding its possible values.

Borgnino et al. (1992) have shown the effect of finite outer scale on the covariances of AA-fluctuations. They concluded that the structure functions are less sensitive to the effect of outer scale than

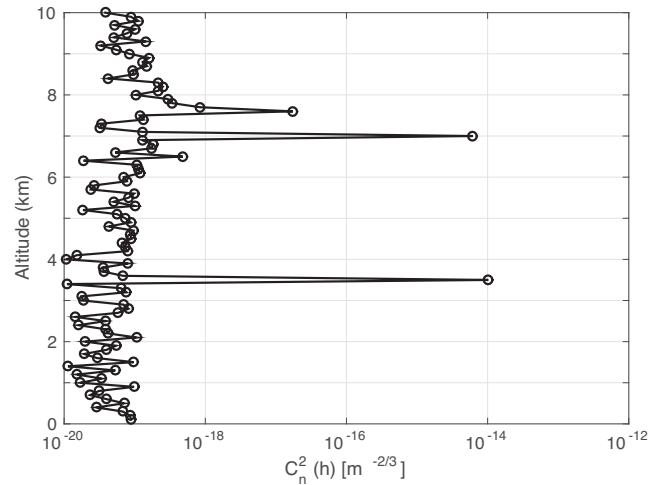


Figure 9. C_n^2 profile retrieved from a structure function obtained by simulation in image plane. The perturbed wavefront was simulated considering two layers localized at altitudes of 3500 and 7000 m, an integrated Fried parameter $r_0 = 6.5$ cm and $\mathcal{L}_0(h) = 3$ m for the two layers.

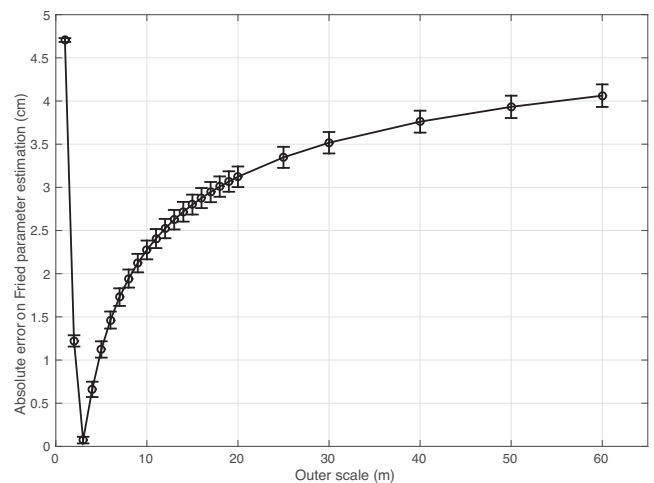


Figure 10. Errors on Fried parameter estimation as a function of outer scale obtained by simulation in image plane. The perturbed wavefront was simulated considering $r_0 = 6.5$ cm, $\mathcal{L}_0 = 3$ m and $h = 3500$ m.

covariance and that for values of \mathcal{L}_0 lower than 4 m, the effect of the finite outer scale on structure functions becomes increasingly important. In our simulation, if one assumes Kolmogorov model and use equation (16) to estimate Fried parameter from AA-fluctuation variance, the resulting value from simulation is $r_{0k} = 12.45 \pm 0.16$ cm which is significantly different from input. To see the effect of neglecting the outer scale until having Kolmogorov regime, one can compute the value of Fried parameter considering equation (15) by varying outer scale values from 1 to 60 m. Errors on Fried parameter estimation are then computed by subtracting the input value. The result is shown in Fig. 10. It is clearly seen that if we want to retrieve Fried parameter from only AA-fluctuation variance, preliminary knowledge of outer scale range is required. Otherwise, the estimated values of r_0 would be wrong especially in the case of finite outer scale values.

5 RESULTS AND DISCUSSIONS

The first light from the instrument was obtained on early 2009. Only the image plane was operating. We presented statistics on Fried parameter measurements between 2010 June and 2012 May in conference proceedings (Ikhlef et al. 2012a,b) using the Kolmogorov model to compute Fried parameter from solar limb motion. First measurements were obtained from the pupil plane on 2011 June. A first attempt to obtain the linear relationship as expected between the AA-fluctuations from image plane (position of the limb) and pupil-plane intensity fluctuations was presented in Irbah et al. (2011). In 2011 however, the instrument was still subject to important mount drift, clearly seen in Fig. 6 of that proceeding, and this may have contaminated our first calibration attempts. Furthermore, to improve again the pupil signal level, we replaced in 2014 the beam splitter and changed the electronic gain of all channels. We are now able to obtain many sequences where no drift signal is seen and for which we are more confident that fluctuations that we observe on both image and pupil planes are due mainly to AA-fluctuations. This allows us to properly cross-calibrate the two observing ways and to compare for the first time the estimates of the turbulence spatial parameters obtained from them.

Here we present some recent results obtained after many improvements of our instrument for minimizing drift and vibrations, improving the signal-to-noise ratio and taking into account the results of our simulations for validating the turbulence parameter extraction procedures. We first give the results for the coherence times obtained directly from the pupil way. Then we present the cross-calibration of the pupil and image planes and compare for the first time the results obtained in both ways for the spatial parameters of turbulence. The following results were obtained at 535.7 nm.

5.1 Coherence time

We present in Fig. 11 an example of intensity fluctuation signal obtained with the 1 mm diameter sub-pupil and the corresponding temporal structure function from which we extract AA-coherence time. The signals from each sub-pupil are divided by the signal which integrates the global flux of the pupil plane; this is similar to a flat-field correction in the image plane. In Fig. 12, we present the daily evolution of measurements performed with the sub-pupil of 1 mm diameter on 2014 October 31. We can see that good observational conditions with higher AA-coherence times are in the early morning, and it degrades with time. This degradation is due to the temperature gradient which generates strong turbulence near the ground. Fig. 13 shows the histogram of measured AA-coherence time values using signals of a sub-pupil of 0.5 mm diameter from 2014 September to 2015 August (about 14 000 measurements). The obtained mean value is 5.34 ms, while the standard deviation is 2.6 ms. This verify a posteriori that our 2000 samples recorded at a rate of one image every 30 ms can be considered as uncorrelated. From the other sub-pupils, the obtained mean values are 5.3 ± 3.2 , 7.5 ± 3.2 and 9.2 ± 3.9 ms for the 0.5, 1 and 2 mm sub-pupils, respectively. The measured AA-coherence time is effectively expected to be a function of diameter of the pupil for given wind speed and outer scale (Ziad et al. 2012).

From equation 10 of Ziad et al. (2012), our measured mean values of the AA-coherence time for the different sub-pupils are compatible within one standard deviation with an average wind speed of about 2.8 ms^{-1} (for a wind direction $\gamma = \frac{\pi}{4}$) and a mean value of 5 m for the outer scale.

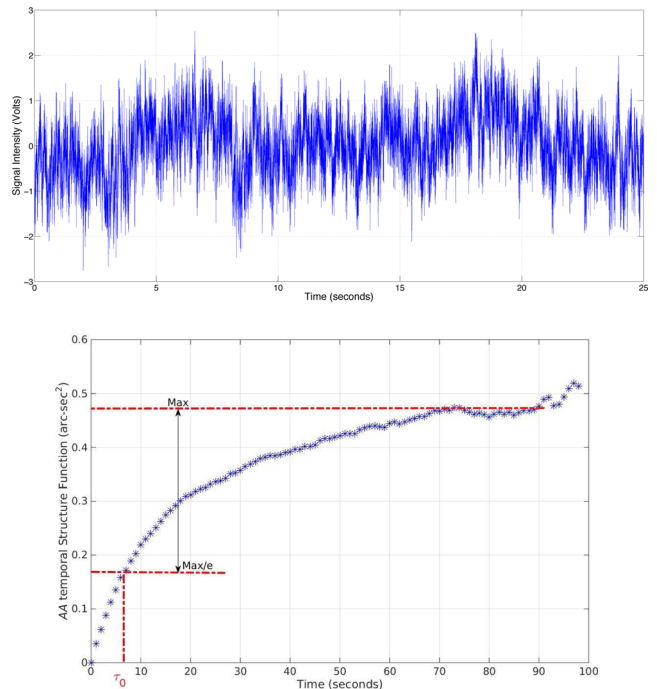


Figure 11. Example of AA-temporal structure function obtained with pupil-plane observation way. The signal was acquired by the 1 mm diameter fibre and its electronics on 2013 June 12.

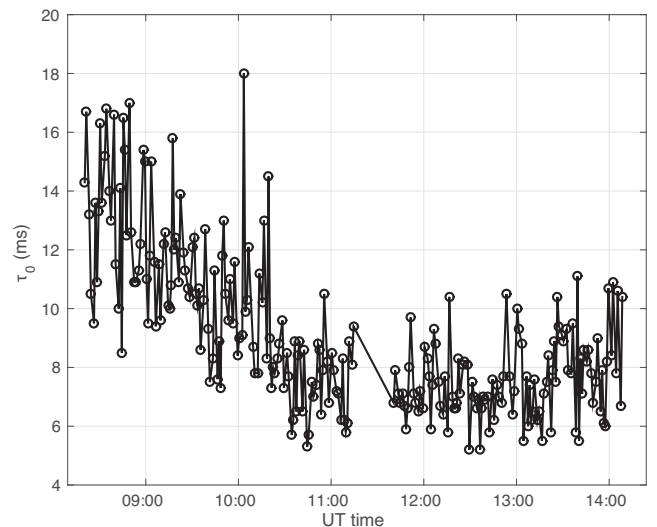


Figure 12. Evolution of measured AA-coherence time on 2014 October 31.

We note that the measured AA-coherence time is different from the coherence time introduced by Roddier, Gilli & Lund (1982) which is the phase coherence time. We could evaluate the Roddier's coherence time either knowing the wind speed profile which is usually given by balloon flights or using the method given by Ziad et al. (2012) which consists in retrieving wind speed from their equation 10 and then use the ratio between the Fried parameter and the wind speed, times a factor 0.31, to estimate the phase coherence time. This supposes that the Fried parameter, the spatial coherence outer scale and the wind speed following the x -direction are known. The mean values of the AA-coherence times given above and the mean values obtained for the spatial parameters (next section) are

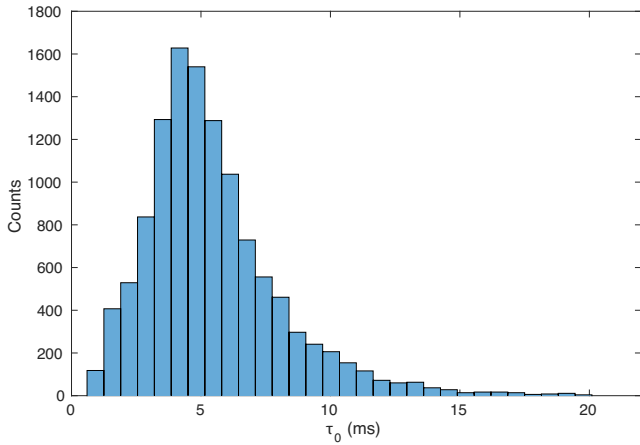


Figure 13. AA-coherence time measurements made by the pupil-plane observation way (0.5 mm sub-pupil) from 2014 September to 2015 August (about 14 000 measurements).

compatible with a phase coherence time ranging between 2.7 and 4.7 ms (for a wind direction $0 \leq \gamma \leq \frac{\pi}{2}$).

5.2 Spatial parameters of turbulence

First we show in Fig. 14 an example of non-linear fitting of structure functions obtained on 2014 October 24 from the image-plane observation way. The error bars represent the statistical error which depends on the considered angular separation and the total number of images; the maximal relative statistical error is about 1.5 per cent corresponding to the maximal angular separation. Other errors may contribute to the total error on the structure function estimation such as the error due the curvature of the limb and the CCD readout noise but they are found negligible as for the MOSP instrument at night (Maire et al. 2007). Assuming the Von Kármán multilayer turbulence model (equation 4), we retrieved the $C_n^2(h)$ and $L_0(h)$ profiles together. For the inversion purpose, the choice of the initial parameters (profiles) and resolution are important to ensure convergence. Like in our two-layer simulation (Section 4), the inverse problem with multiple layers is ill-posed in the sense that several solutions, i.e. $C_n^2(h)$ and $L_0(h)$ profiles, are able to reproduce equally well the observed structure function within its error bars. We have tested the

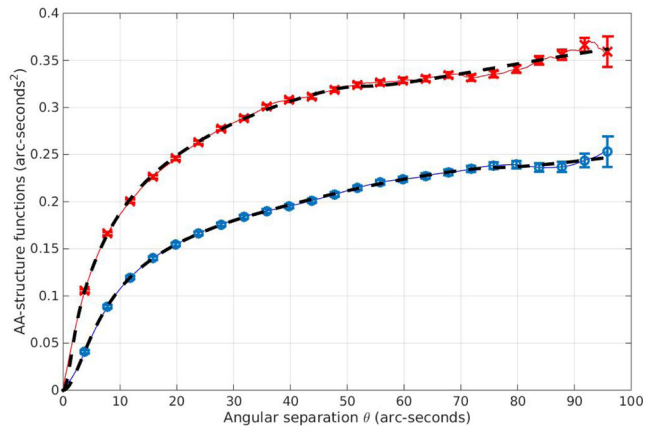


Figure 14. Experimental structure functions obtained on 2014 October 24 at 08:27 UT (red crosses) and 8:11 UT (blue circles). The non-linear curve fitting (dashed lines) allowed us to extract spatial parameters.

inversion starting with a constant value for the C_n^2 profile but keeping the L_0 one close to the solution. In this case, we are still able to converge to the solution for $C_n^2(h)$. On the other hand, doing the opposite ($L_0(h)$ constant and $C_n^2(h)$ close to its solution) or starting with two constant profiles does not allow us to converge to the solution. Here an a priori is introduced by starting the procedure with parametric models for realistic daytime turbulence profiles $C_n^2(h)$ and $L_0(h)$. For $C_n^2(h)$, we started the inversion process using the Hufnagel–Valey model (Hufnagel 1974; Valey 1980):

$$C_n^2(h) = 0.00594 \left(\frac{V}{27} \right)^2 (10^{-5}h)^{10} \exp\left(-\frac{h}{1000}\right) + 2.710^{-16} \exp\left(-\frac{h}{1500}\right) + A \exp\left(-\frac{h}{100}\right), \quad (25)$$

where h is the altitude (in m), V is the rms wind speed at high altitude taken equal to 21 m s^{-1} and A is a constant defining the turbulence strength at ground level; it is taken equal to $1.7 \times 10^{-14} \text{ m}^{-2/3}$ for daytime turbulence.

For the outer scale profile $L_0(h)$, we started the inversion process using the model proposed by Coulman et al. (1988):

$$L_0(h) = \frac{4}{1 + \left(\frac{h-8500}{2500} \right)^2}. \quad (26)$$

Fig. 15 presents the profiles obtained from the structure functions of Fig. 14, and integrated parameters using equations (11) and (12) are $r_0 = 7.9 \text{ cm}$, $\mathcal{L}_0 = 6.2 \text{ m}$ for the first one (blue curve) and $r_0 = 5.5 \text{ cm}$, $\mathcal{L}_0 = 6.1 \text{ m}$ for the second one (red curve). We notice that most of the turbulence is localized in the surface layer; this is due to air heating by the solar rays near the ground. For ground layers and a telescope diameter of 25 cm, simulations show that there is a limit around $L_0 = 4 \text{ m}$ above which the instrument is not sensitive. In other words, for greater values of L_0 in the ground layers, the observed structure function will not change significantly in the range 0–96 arcsec sensed by MISOLFA. This implies that the integrated values obtained should be considered as lower limits only. If we fix the L_0 profile, then the inverse problem of retrieving the C_n^2 profile (equation 4) becomes linear and we can compute the optimal resolution kernels (Backus & Gilbert 1968) for realistic uncertainties on the observed structure function. This provides intrinsic resolution of the inverse problem for a given L_0 profile and clearly shows that MISOLFA can provide information up to at least 20 km with a resolution ranging from about 2 km at an altitude of 2 km up to 6 km at an altitude of 20 km. For lower layers, the resolution reachable on the C_n^2 profile will be more sensitive to the real L_0 profile. This led us to choose an altitude sampling step of 100 m in this region of the atmosphere and a relatively higher sampling (1 km) in the free atmosphere. In a future work, we plan to test the use of an iterative process that would adapt the number of layers at each step as the L_0 profile evolves.

As described in Section 3.2.2, spatial parameters from pupil plane can also be estimated. For that a calibration of pupil intensity fluctuations (in volts) according to AA-fluctuations (in arcseconds) is needed. In Fig. 16, we present the correlation between the two entities. A linear fit leads to a calibration of intensity fluctuations in arcseconds. Each signal from the sub-pupils is calibrated separately because each acquisition channel has its own amplification device with different gains and offsets. This calibration is made every time the gains are changed. The resulting signals are used to estimate spatial parameters.

To compare estimated parameters between image and pupil planes, we show first in Fig. 17 daily evolution of simultaneous

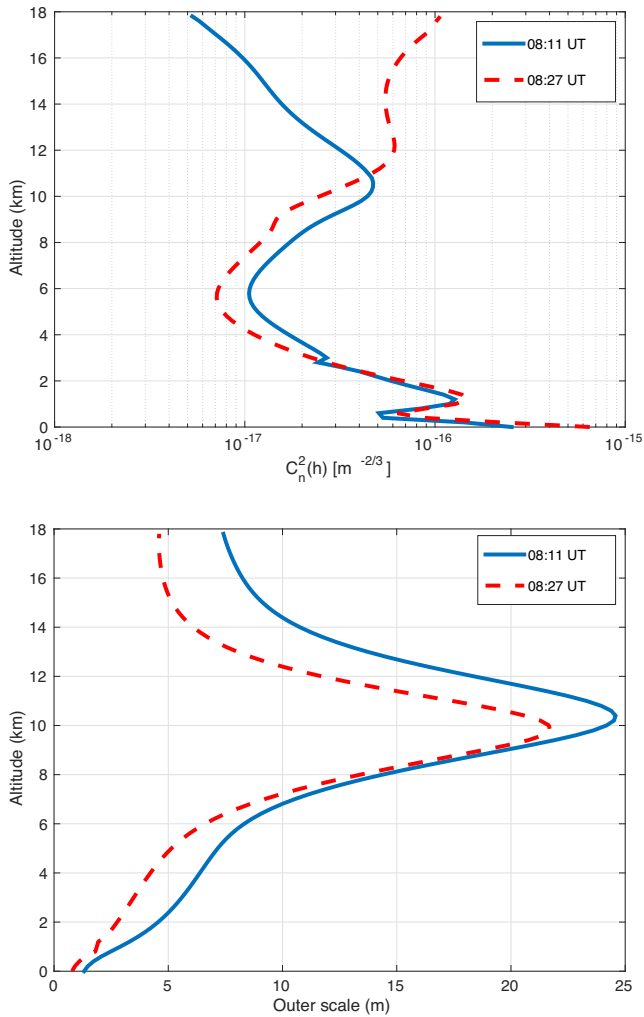


Figure 15. $C_n^2(h)$ and $L_0(h)$ profiles retrieved from structure functions obtained on 2014 October 24.

r_0 measurements from the pupil and image planes. The estimations from image motion (black circles) are obtained considering the Von Kármán model (equation 15). The values of L_0 are retrieved from the integration of the $L_0(h)$ profiles weighted by the $C_n^2(h)$ profiles (equation 12). Fig. 18 represents the latter outer scale estimations and simultaneously estimations from pupil plane by a numerical resolution of equation (19). The mean values from the two curves are 11.2 ± 5.1 and 8.3 ± 7.0 m for the outer scale values from the image and pupil planes, respectively. These estimates are in good agreement and give the same order of outer scale values.

One can notice that pupil-plane observations are in good agreement with estimations from integrated $C_n^2(h)$. We can also see that good seeing conditions are observed early in the morning. We believe that most reliable from these estimations is made from pupil plane because it is based on a differential estimation method. But its disadvantage is that it is sensitive to noise in the sub-pupils (0.5 mm) used during the estimation and because of filtering due to the slit (see Section 2.2), there is a limitation in observed atmospheric perturbation and so Fried parameter estimation. In Fig. 17, we can see that the estimations from image motion give lower values compared to the two other estimations. This is because it is based on the variance which is overestimated in the presence of drift (or drift residuals after some corrections). On the other hand, this estimation

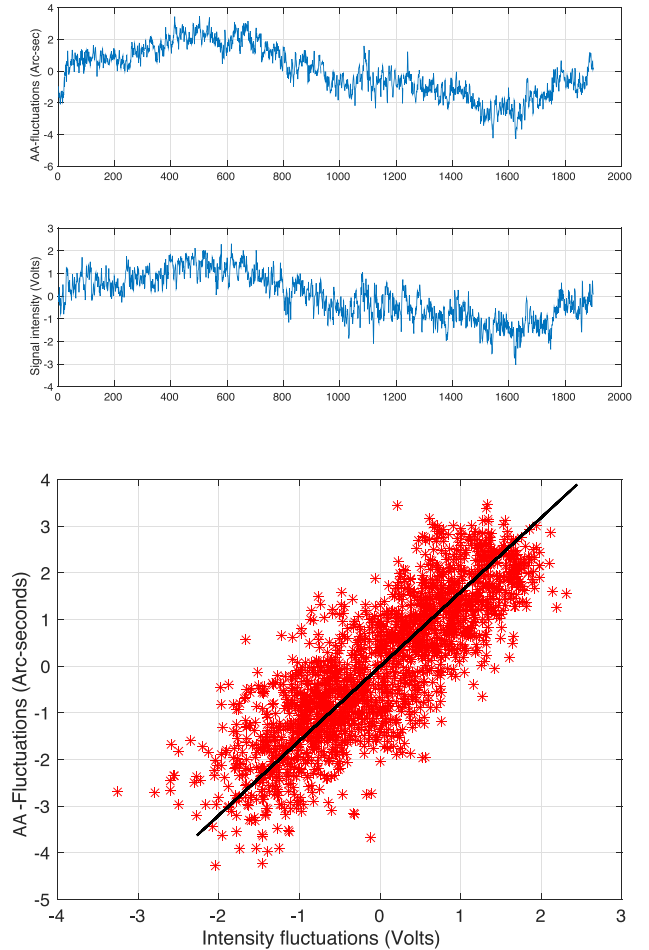


Figure 16. Correlation between temporal evolution of AA-fluctuations from solar limb in image plane (top), as a function of pupil-plane temporal signal (bottom). The data were recorded on 2014 October 24; the pupil signal was obtained with the sub-pupil of 1 mm diameter.

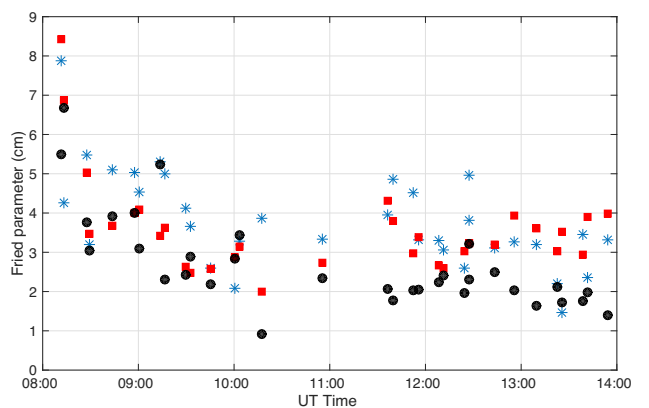


Figure 17. Fried parameter measurements from the pupil plane (red squares), image agitation (black circles) and from integrated $C_n^2(h)$ profiles (blue stars) of the image-plane observation way on 2014 October 24.

method uses an outer scale value retrieved from profiles. For the inversion technique, because we have to retrieve the two profiles ($C_n^2(h)$ and $L_0(h)$) together, the solution is not unique and can give different values of integrated parameters. Indeed, we simulated a structure function with the profiles of equations (25) and (26) in

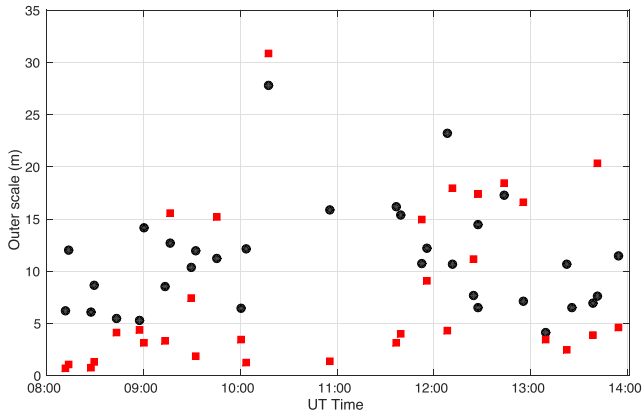


Figure 18. Outer scale measurements from the pupil plane (red squares) and from the integration of the $L_0(h)$ profiles (black circles) of the image plane; observations were performed on 2014 October 24.

order to test the inversion procedure. It gives good results (close to input parameters), but a small variation in retrieved profiles gives slightly different values of integrated parameters. Also the use of different resolutions in altitude gives similar profiles but different values of integrated parameters. Maire et al. (2007) did the same thing in order to test the simulated annealing inversion technique and concluded that the results are more reliable when unknowns are only $L_0(h)$.

Considering the pupil-plane observation way, we evaluated the mean values of the spatial parameters over one year of observations. We obtained a median value of Fried parameter of 3.3 cm, while the outer scale median value is about 6.3 m. The mean Fried parameter estimated using MISOLFA image way over 2 years has already been used for the solar ground-based astrometric measurements carried at Calern Observatory (Mefftah et al. 2014, 2015). At this time, only the image way was operating. In the present work, we obtain similar values for the Fried parameter and our results are further validated by analysing also the pupil way of the instrument.

We have demonstrated that we have the capacity with MISOLFA not only to estimate the integrated values but also the $C_n^2(h)$ and $L_0(h)$ profiles. Simulations have shown that this approach could give even better results than fitting the structure function for the integrated parameters. When confronted to the observations, this approach is however less robust and it is hard to assure good convergence in all conditions. A calibration with another instrument would help to fully exploit this additional capacity of retrieving these profiles.

6 CONCLUSION

A generalized daytime turbulence monitor is presented in this paper allowing estimation of both spatial and temporal parameters of optical turbulence. It is based on the statistics of AA-fluctuations observed in both image and pupil planes. On top of what would give the use of SHABAR and S-DIMM instruments (r_0 , $C_n^2(h)$), we are able, with a single instrument, to estimate the outer scale and characteristic time of turbulence. This is an important new tool for site testing and for real-time atmospheric monitoring during high-resolution ground-based solar observations. It has been shown by both numerical simulations and from real data that Fried parameter for daytime observations can be deduced from AA-fluctuation variance considering the Von K arm an model and introducing a finite

value of outer scale. This confirms the theoretical results obtained by Borgnino et al. (1992).

Using a grid ranging from 100 m in the planetary layer up to 1 km in the free atmosphere, we have also shown from both simulations and real data that MISOLFA allows us to retrieve the atmospheric structure constant $C_n^2(h)$ and outer scale $L_0(h)$ profiles. First simultaneous estimated profiles obtained from observations made in 2014 October are presented, and we have shown that the integrated parameters deduced from these profiles are compatible with the ones deduced for the variance of the limb motion if one takes into account a finite value of outer scale.

We presented the first fully calibrated measurements from the pupil-plane observation way after many improvement in the data quality, data acquisition systems and telescope guiding. Using its pupil-plane observation way, we obtained an estimation of turbulence AA-coherence time τ_{0AA} and its statistic over one year. We obtained a mean value of about 5 ms with larger values up to 18 ms typically obtained in early morning.

The spatial parameters r_0 and \mathcal{L}_0 at 535 nm have also been deduced from the use of two sub-pupils and have been found in good agreement with the measurements made directly in the image plane. This good agreement found between the image- and pupil-plane observation ways constitutes a first internal calibration of the instrument not available on other systems. It also validates our parameter extraction procedures. We have shown from simulations that retrieving first the profiles $C_n^2(h)$ and $L_0(h)$ from the structure function and then integrating them to retrieve the integrated parameters is the most reliable procedure. We were able to apply it to real data acquired in good conditions and to successfully compare the results with the ones extracted from the pupil way. The inversion procedure to solve the integral equation remains however an ill-posed problem sensitive to the choices made for the initial parameters. Our conclusion, at this stage of our work, is that the most robust procedure is to use both observing ways to cross-validate our results concerning the spatial parameters of turbulence.

MISOLFA is a complex instrument, and some of its initial specifications have been made to allow testing various theoretical approaches of turbulence parameter extraction. The reflected images were not fully exploited because a coating stable in time could be obtained only with a ratio between the direct and reflected intensities less than initially specified. Since the two limbs coming from the two sides of the solar disc are separated by more than 1900 arcsec, we could use them to compute a structure function with large separation allowing in principle to reach the saturation even for the low-altitude layers. The use of the different size sub-pupils to estimate the outer scale via equation (23) was not successful probably because their differences in size were probably not large enough. The ratio between covariance and variance for two sub-pupils of the same size however gives results in good agreement with results from the image way. Finally, we note that we have not used the slit wheel, the purpose of which was to allow us to test different filterings in the pupil way. We needed to accumulate data without changing the configuration and the initial slit choice revealed itself appropriate. If not filtered, instrument vibrations could be interpreted as a signal coming from the turbulence and therefore bias the results. An efficient method to correct from vibrations is the use of differential observations (case of the DIMM and PML). In MISOLFA, the same is made in the pupil plane where we look at the correlations between intensity fluctuations coming from two sub-pupils both normalized by the global flux. In this way, the vibrations should not affect the measurements. In the image way however, the vibrations are not taken into account. This, in principle, could have been achieved by

looking at the two opposite limbs which are affected in the same way. But again, the poor signal-to-noise ratio of the reflected limb image prevented us to apply this method at this stage. An alternative could be to measure the vibrations with accelerometers and filter their frequencies which are expected to lie in the lower part of the absolute motion spectrum (below 1 Hz; Martin 1987). Part of the differences sometimes obtained between the image and pupil ways may come from these different sensitivities to vibrations.

The two observing ways of MISOLFA are now fully operational in their actual configuration. Our results could however still be consolidated and probably improved by calibrating it with other instruments such as S-DIMM or with similar instruments such as MOSP or PML with adaptation for solar observations. A simultaneous measurement of vertical distribution of temperature and wind speed with altitude using balloon flight would also be useful. Measurement of structure constant of temperature fluctuations ($C_T^2(h)$) coupled with mean values of temperature and pressure distribution with altitude would lead to an independent estimate of the energy distribution $C_n^2(h)$ and the size of the isoplanatic patch θ_0 (Roddier 1981). Furthermore, the wind speed distribution would give access to phase coherence time.

In a future work, we intend to cross-calibrate MISOLFA with other turbulence monitors in order to further consolidate our results not only for the temporal variation of the turbulence parameters but also for their fully calibrated absolute values.

ACKNOWLEDGEMENTS

We thank the anonymous referee for careful and helpful advice and comments. This work is dedicated to the memory of Francis LA-CLARE who was at the origin of the ground based solar astrometry program at Calern Observatory. This project is supported by the Centre National des Etudes Spatiales (CNES) and the Programme National Soleil-Terre (PNST).

REFERENCES

Acton D. S., 1995, *Appl. Opt.*, 34, 4526
 Assus P., Borgnino J., Martin F., Bouzid A., Chibani M., Irbah A., Seghouani N., 2002, in Vernin J., Benkhaldoun Z., Muñoz-Tuñón C., eds, *ASP Conf. Ser. Vol. 266, Astronomical Site Evaluation in the Visible and Radio Range*. Astron. Soc. Pac., San Francisco, p. 134
 Avila R., Ziad A., Borgnino J., Martin F., Agabi A., Tokovinin A., 1997, *J. Opt. Soc. Am.*, 14, 11
 Backus G. E., Gilbert F., 1968, *Geophys. J. R. Astron. Soc.*, 16, 169
 Beckers J. M., 1999, in Schmieder B., Hofmann A., Staude J., eds, *ASP Conf. Ser. Vol. 184, Third Advances in Solar Physics Euroconference: Magnetic Fields and Oscillations*. Astron. Soc. Pac., San Francisco, p. 309
 Beckers J. M., 2001, *Exp. Astron.*, 12, 1
 Beckers J. M., Mason J., 1998, *Proc. SPIE*, 3352, 858
 Beckers J. M., Liu Z., Jin Z., 2003, *Proc. SPIE*, 4853, 273
 Berdja A., 2007, PhD thesis, Univ. Nice Sophia-Antipolis
 Berdja A., Irbah A., Borgnino J., Martin F., 2004, *Proc. SPIE*, 5237, 238
 Berkefeld T. et al., 2010, *Proc. SPIE*, 7733, 77334I
 Borgnino J., 1978, PhD thesis, Univ. Nice Sophia-Antipolis
 Borgnino J., 1990, *Appl. Opt.*, 29, 1863
 Borgnino J., Martin F., 1977, *J. Opt. (Paris)*, 8, 319
 Borgnino J., Martin F., 1978, *J. Opt. (Paris)*, 9, 15
 Borgnino J., Ceppatelli G., Ricort G., Righini A., 1982, *A&A*, 107, 333
 Borgnino J., Martin F., Ziad A., 1992, *Opt. Commun.*, 91, 267

Borgnino J., Berdja A., Ziad A., Maire J., 2007, in Cherubini T., Businger S., eds, *Proc. Symp. on Seeing*
 Bouzid A., Irbah A., Borgnino J., Lantéri H., 2002, in Vernin J., Benkhaldoun Z., Muñoz-Tuñón C., eds, *ASP Conf. Ser. Vol. 266, Astronomical Site Evaluation in the Visible and Radio Range*. Astron. Soc. Pac., San Francisco, p. 64
 Conan R., 2000, PhD thesis, Univ. Nice Sophia-Antipolis
 Conan R., Borgnino J., Ziad A., Martin F., 2000, *J. Opt. Soc. Am. A*, 17, 1807
 Coulman C. E., Vernin J., Coquegniot Y., Caccia J. L., 1988, *Appl. Opt.*, 27, 155
 Djafer D., Irbah A., 2012, *Sol. Phys.*, 281, 863
 Fried D. L., 1965, *J. Opt. Soc. Am. A*, 56, 1372
 Fried D. L., 1975, *Radio Sci.*, 10, 71
 Gao B. C., 1993, *Remote Sens. Environ.*, 43, 23
 Hestroffer D., Magnan C., 1998, *A&A*, 333, 338
 Hufnagel R. E., 1974, 'Variations of atmospheric turbulence,' in *Optical Propagation through Turbulence*, OSA Technical Digest Series, Optical Society of America, Washington, D.C., Paper WA1
 Ikhlef R. et al., 2012a, in Faurobert M., Fang C., Corbard T., eds, *EAS Publ. Ser. Vol. 55, Understanding Solar Activity: Advances and Challenges*, p. 369
 Ikhlef R. et al., 2012b, *Proc. SPIE*, 8444, 84446C
 Irbah A., Borgnino J., Laclare F., Merlin G., 1994, *Sol. Phys.*, 149, 213
 Irbah A. et al., 2010, *Proc. SPIE*, 7735, 77356F
 Irbah A. et al., 2011, *Proc. SPIE*, 8178, 81780A
 Kawate T., Hanaoka Y., Ichimoto K., Miura N., 2011, *MNRAS*, 416, 2154
 Kellerer A., Gorceix N., Marino J., Cao W., Goode P. R., 2012, *A&A*, 542, A2, 10
 Laclare F., 1983, *A&A*, 125, 200
 Lakhall L., Irbah A., Bouzaria M., Borgnino J., Laclare F., Delmas C., 1999, *A&AS*, 138, 155
 Liu Z., Beckers J. M., 2001, *Sol. Phys.*, 198, 197
 Maire J., Ziad A., Borgnino J., Martin F., 2007, *MNRAS*, 377, 1236
 Martin H. M., 1987, *PASP*, 99, 1360
 Martin F., Tokovinin A., Agabi A., Borgnino J., Ziad A., 1994, *A&AS*, 108, 173
 Meftah M. et al., 2014, *A&A*, 569, A60
 Meftah M. et al., 2015, *ApJ*, 108, 173
 Morand F., Delmas C., Corbard T., Chauvineau B., Irbah A., Fodil M., Laclare F., 2010, *C. R. Phys.*, 11, 660
 Moussaoui R., Irbah A., 2000, *Ap&SS*, 273, 25
 Nakajima T., 1988, *J. Opt. Soc. Am. A*, 5, 1477
 Roddier F., 1981, *Progress in Optics*, Vol. 19. North-Holland, Amsterdam, p. 281
 Roddier F., Gilli J. M., Lund G., 1982, *J. Opt. (Paris)*, 13, 263
 Sarazin M., Roddier F., 1990, *A&A*, 227, 294
 Scharmer G. B., van Werkhoven T. I. M., 2010, *A&A*, 513, A25
 Schmidt J. D., 2010, *Numerical Simulation of Optical Wave Propagation*. SPIE, Bellingham
 Schmidt D., Berkefeld T., Heidecke F., Fischer A., von der Lühe O., Soltau D., 2014, *Proc. SPIE*, 9148, 1
 Seghouani N., Irbah A., Borgnino J., 2002, in Vernin J., Benkhaldoun Z., Muñoz-Tuñón C., eds, *ASP Conf. Ser. Vol. 266, Astronomical Site Evaluation in the Visible and Radio Range*. Astron. Soc. Pac., San Francisco, p. 36
 Valey C. G., 1980, *Appl. Opt.*, 19, 574
 Ziad A., Borgnino J., Martin F., Agabi A., 1994, *A&A*, 282, 1021
 Ziad A., Conan R., Tokovinin A., Martin F., Borgnino J., 2000, *Appl. Opt.*, 39, 30
 Ziad A., Borgnino J., Dali-Ali W., Berdja A., Maire J., Martin F., 2012, *J. Opt.*, 14, 8
 Ziad A. et al., 2013, in Esposito S., Fini L., eds, *Proc. Third AO4ELT Conf.*

This paper has been typeset from a $\text{\TeX}/\text{\LaTeX}$ file prepared by the author.